Journal of Materials Chemistry B

ROYAL SOCIETY OF CHEMISTRY

PAPER

Cite this: *J. Mater. Chem. B*, 2021, **9**, 5055

Impact of the chain length on the biodistribution profiles of PEGylated iron oxide nanoparticles: a multimodal imaging study†

Dimitri Stanicki,*[a] Lionel Larbanoix,[b] Sébastien Boutry,[b] Thomas Vangijzegem,[a] Indiana Ternad,[a] Sarah Garifo,[a] Robert N. Muller[ab] and Sophie Laurent*[ab]

Received 16th March 2021,
Accepted 26th May 2021

DOI: 10.1039/d1tb00573a

rsc.li/materials-b

Bimodal sub-5 nm superparamagnetic iron oxide nanoparticles (SPIO-5) coated with polyethylene glycol of different chain lengths (*i.e.* PEG-800, -2000 and -5000) have been prepared and characterized. Fluorescence properties have been obtained by mean of the grafting of a near-infrared-emitting dye (NIR-dye) onto the surface of the oxide, thanks to the carboxylic acid functions introduced towards an organosilane coating. Such modification allowed us to follow *in vivo* their biodistribution and elimination pathways by T_1–w and T_2–w high-field magnetic resonance imaging (MRI), as well as by optical and optoacoustic imaging. Interestingly, it has been highlighted that for a given composition, the thickness of the coating strongly influences the pharmacokinetic properties of the administrated SPIO-5.

Introduction

In the field of nanotechnology, the last decades have witnessed the emergence of many nanosystems exhibiting customized properties which can find major interest for many applications. Among the existing developed nanomaterials, superparamagnetic iron oxide nanoparticles (SPIO; especially maghemite and magnetite) have emerged as promising candidates thanks to their remarkable magnetic properties, especially for biomedical applications where their efficiency as a contrast enhancer for magnetic resonance imaging (MRI) has been widely documented.[1–3] Though such iron oxide-based systems were clinically used until the late 90s,[4,5] their success has been hampered firstly by their "signal-destructive behavior" which darkens their accumulation area, and is prone to the so-called "blooming-effect", and secondly by the competition of the existing T_1 contrast agents (gadolinium complexes) which exhibit signal-brightening properties that can, in some cases, facilitate the establishment of a diagnosis.[6–8] However, one must stress that, depending on the application, the usefulness of gadolinated compounds may be limited because of their particular pharmacokinetic properties. It is the case, as an example, for MR angiography (*i.e.* MRA) for which rapid extravasation and renal clearance of clinically used complexes do not allow long-time acquisition.[9,10] Interestingly, several recent studies[6,11–14] have shown that such a brightening effect can be obtained for spherical SPIO below a critical size (*i.e.* 5 nm), highlighting the potential of such systems for vascular imaging or solid tumor enhanced permeability and retention (EPR)-targeting. More than the crystal size, it should be noticed that this characteristic remains true only for monocore systems. Indeed, it is well documented that particle agglomeration induces a dramatic increase of the transverse to longitudinal relaxivity ratio (r_2/r_1) that leads to an emphasis of the T_2 effect at the expense of the T_1 one.[15] In addition, their agglomeration at the cellular level triggers the recognition followed by the clearance by the mononuclear phagocyte system (MPS).[16] Consequently, besides inherent physico-chemical properties (*i.e.* shape, size, composition, polydispersity, ...), the stability of the systems appears to be a critical parameter that strongly determines the particle's ability to circulate in the bloodstream for a long time.

Former studies described excellent properties obtained by using a PEG-based coating, as a consequence of its hydrophilicity, biocompatibility and stealth properties conferred to the nano-system.[17–19] It is already well documented that a PEG-based coating, which helps to reduce non-specific blood protein adsorption, acts as a protective layer regarding phagocyte adhesion.[20–23] If some reports already studied the influence of the PEG composition (length, charge, topology,...) on the biological behavior of associated particles (liposomes, polymeric vesicles, inorganic nanoparticles,...),[24–29] most of these studies focused on *in vitro* models (protein interactions, cellular uptake, molecular response and toxicity), and *in vivo* imaging data are still missing, especially for sub-10 nm SPIO.

[a] *General, Organic and Biomedical Chemistry Units, NMR and Molecular Imaging Laboratory, University of Mons, B-7000 Mons, Belgium. E-mail: dimitri.stanicki@umons.ac.be, sophie.laurent@umons.ac.be*
[b] *Center for Microscopy and Molecular Imaging, University of Mons, B-6041 Gosselies, Belgium*

† Electronic supplementary information (ESI) available. See DOI: 10.1039/d1tb00573a

As the surface composition may have an influence on the blood circulation time and owing to the growing interest for T_1-active-SPIO for MRA applications, we were interested in determining the effect of linear PEG of various molecular weights (*i.e.* methoxylated PEG-800, -2000 and -5000) on the biodistribution profiles of 5 nm-SPIO (SPIO-5) through an imaging approach. A combination of the SPIO-5 with near-infrared (NIR) emitting dye allowed us to bring together complementary data resulting from different imaging modalities, *i.e.* T_1 and T_2-weighted MRI, near-infrared (NIR) fluorescence imaging (FLI) and multi-spectral optoacoustic tomography (MSOT). While MRI and FLI are well known, MSOT is an emerging imaging modality that provides a very high and interesting performance.[30] Indeed, optoacoustic (or photoacoustic) imaging combines the benefits of fluorescence and ultrasound imaging (*i.e.* high spatio-temporal resolution, high sensitivity, high contrast between numerous chromophores, and deep tissue penetration (up to several centimeters)). Moreover, MSOT provides up to 10 Hz imaging rate, which is very fast and, thus, close to real time imaging.

Experimental section

Materials

Ferric chloride solution ($FeCl_3$, 45%), ferrous chloride tetrahydrate ($FeCl_2{\cdot}4H_2O$, $>99\%$), 2-propanol, potassium hydroxide and sodium hydroxide were purchased from Fluka (Belgium). Diethylene glycol (DEG), *N*-(3-dimethylaminopropyl)-*N*′-ethylcarbodiimide hydrochloride (EDC·HCl), *N*-boc-1,4-butanediamine, dimethylformamide (DMF), acetone, diethylether, glacial acetic acid, (3-bromopropyl)trimethylammonium bromide, phosphorus oxychloride, 3-(4-hydroxyphenyl)propionic acid, 4-hydrazinobenzene sulfonic acid, 3-methyl-2-butanone, aniline, cyclohexanone and anhydrous tetrahydrofuran (THF), and human serum albumin (HSA) were purchased from Sigma-Aldrich (Belgium). 3-(triethoxysilyl)propyl succinic anhydride (TEPSA) was purchased from ABCR (Germany). α-Methoxy-ω-amino poly(ethylene glycol) 800, 2000 and 5000 were purchased from Iris Biotech GMBH (Germany).

All the materials mentioned above were used without further purification. Membranes (MWCO = 30 000 Da) for ultrafiltration were purchased from Millipore (USA).

Characterization techniques

Transmission electron microscopy (TEM) was used to obtain detailed information about the morphology and the size of the samples and was carried out using a Fei Tecnai 10 microscope (Oregon, USA) operating at an accelerating voltage of 80 kV. The samples were prepared by placing a drop of diluted suspension on a copper-grid (300 mesh), allowing the liquid to dry in air at room temperature. The statistical analysis of the TEM images was performed by iTEM (Germany) on multiple images for each sample. The mean diameter, the standard deviation, and the polydispersity index (PDI) were calculated by measuring the particle diameter. The number of nanoparticles counted ranged from 500 to 700. Measurements of the size distribution and the zeta potential of the nanoparticles suspended in aqueous medium were performed on a Zetasizer Nano ZS (Malvern Instruments, United Kingdom) using laser He–Ne (633 nm). Nuclear Magnetic Relaxation Dispersion (NMRD) profiles were recorded with a field cycling relaxometer (STELAR, Mede, Italy) measuring the longitudinal relaxation rates (R_1) in a magnetic field range extending from 0.24 mT to 1 T. The temperature of the samples was adjusted to 37 °C with a precision of 0.1 °C. The theoretical adjustment of the NMRD profiles was performed with classical relaxation models. Longitudinal (R_1) and transverse (R_2) relaxation rate measurements at 0.47 and 1.41 T were obtained on Minispec mq 20 and mq 60 spin analyzers (Bruker, Germany), respectively. The relaxation rates were measured as a function of the iron molar concentration at 0.47 and 1.41 T in order to calculate the r_1 and r_2 relaxivities (defined as the enhancement of the water proton relaxation rate in 1 mmol l^{-1} solution of contrast agents). The relaxivities were calculated as the slope of relaxation rate (R^{i}_{obs}) *versus* iron concentration according to the equation:

$$R_i^{obs} = \frac{1}{T_i^{obs}} = r_i[\mathrm{Fe}] + \frac{1}{T_i^{dia}}$$

r_i being the relaxivities and T_i^{dia} being the proton relaxation times in aqueous solutions without nanoparticle. The total iron concentration was determined by measuring the longitudinal relaxation rate R_1 according to the method previously described. Briefly, the samples were mineralized by microwave digestion (MLS-1200 Mega, Milestone, Analis, Belgium) and the R_1 value of the resulting solutions was recorded at 0.47 T and 37 °C, which allowed the determination of iron concentration using the equation:

$$[\mathrm{Fe}] = (R_1^{sample} - R_1^{dia}) \times 0.0915$$

where R_1^{dia} (s^{-1}) is the diamagnetic relaxation rate of acidified water (0.36 s^{-1}) and 0.0915 (s mM) is the slope of the calibration curve.

Thermogravimetric analyses (TGA) were conducted on a TA Q5000 system (TA Instruments, USA). Before analysis, the samples were first heated at 80 °C during 24 h to eliminate free water. The mass loss of the pre-dried samples was monitored under nitrogen from room temperature to 120 °C at a heating rate of 10 °C min^{-1}. After an isotherm at 120 °C under nitrogen during 10 min to remove the bound water, the samples were heated from 120 °C to 600 °C at a heating rate of 10 °C min^{-1} under air.

The organic and inorganic contents were determined from the weight loss on the TGA curves. We deduced the number n_{TEPSA} of organosilane molecules grafted to the USPIO nanoparticle by:[31]

$$\frac{\text{org. wt\%}}{\text{inorg. wt\%}} = \frac{n_{TEPSA} \times M_w^{TEPSA}}{M_w^{SPIO}}$$

where M_w^{SPIO} is the molar mass of the particle estimated by:

$$M_w^{SPIO} = \frac{4}{3}\pi R^3 \times N_A \times \rho$$

where N_A is the Avogadro number and ρ the mass density of Fe_3O_4 = 5180 kg m^{-3} and R the particle radius (2.45 nm determined from TEM analysis). For SPIO nanoparticles firstly coated with TEPSA then coupled to polymer chains, the organic content measured by TGA is the sum of the two components:

$$\frac{\text{org. wt\%}}{\text{inorg. wt\%}} = \frac{n_{\text{TEPSA}} \times M_w^{\text{TEPSA}}}{M_w^{\text{SPIO}}} + \frac{n_{\text{polymer}} \times M_w^{\text{polymer}}}{M_w^{\text{SPIO}}}$$

As the grafting density of the silane should not be affected by the coupling reaction with the polymer, the weight ratio of TEPSA relative to SPIO was considered constant for all samples.

The emission spectra were recorded at room temperature on a PerkinElmer LS 55 spectrofluorometer (PerkinElmer, USA). The excitation and emission slits were set at 10 nm while the scanning rate was set at 200 nm min^{-1}. ^{1}H NMR spectra were obtained using a Bruker Avance instrument (500 MHz) and chemical shifts (d) are given in ppm using tetramethylsilane (TMS) as an internal reference. The following abbreviations are used: br for broad, s for singlet, d for doublet, t for triplet, q for quadruplet, and m for multiplet.

Fluorescence emission were also analyzed using an *in vivo* fluorescence imaging scanner (PhotonImager Optima, Biospace Lab, France) in order to validate their utilities in closer conditions of the *in vivo* imaging procedure. A 96 well white plate was filled with 100 μl of SPIO at different concentrations ranging from 0.1 mM to 5 mM. Fluorescence was measured with 25 nm band-pass (BP) filters centered on 737 nm for excitation and 797 nm for emission. Fluorescence intensities were measured using M3Vision software (Biospace Lab) by drawing ROI around each well, and it was expressed as photons per second per square centimeter per steradian (ph/s/cm^2/sr).

Optoacoustic emission spectra were recorded in the *in vivo* MSOT scanner (InVision 256-TF, iThera Medical, Germany) using a durable fantom (iThera Medical). The left well was filled with saline during the whole experiment and was used as the baseline. The right well was filled successively with a different concentration of each SPIO and washed in between each measurement. The fantom was set in the fantom holder and positioned in the motorized stage inside the imaging chamber. Samples were excited from 660 nm to 930 nm by 5 nm steps. Images were reconstructed using a model-based algorithm in viewMSOT software (iThera Medical) and optoacoustic signal intensities were extracted in MSOT arbitrary unit (a.u.).

MR images of samples were acquired in a Biospec (9.4T) from Bruker (Germany), using a 60 mm diameter volume coil so that all samples were scanned at once (all in the same field of view) for each sequence used. Contrast-influencing imaging parameters are the same as those used for *in vivo* MRI acquisitions. Main sequences were T_1-weighted fast imaging with steady-state free precession (FISP 3D; TR/TE = 4.4/1.5 ms, FA = 15°, 5 averages, 153 × 146 × 1000 micrometers resolution) and T_2-weighted rapid acquisition with relaxation enhancement (RARE 2D; TR/TE = 2000/17 ms, 5 averages, 1 mm slice thickness, 215 × 219 micrometers resolution). Images were collected from the ParaVision 5.1 software.

Synthesis of magnetic nanoparticles (SPIO)

Magnetic nanoparticles were prepared by co-precipitation of iron salts in DEG according to a protocol previously described. Briefly, a mixture of ferrous chloride tetrahydrate salt (45 mmol; 8.9 g) and ferric chloride (45%; 37 mmol; 9.1 ml) in DEG (250 ml) was heated at 170 °C under a nitrogen atmosphere and under stirring. After 15 min at that temperature, solid sodium hydroxide (15 g) was added in order to prevent any dilution. The solution was stirred for 1 h at 170 °C. The mixture was then cooled, and the magnetic particles were isolated from the solution by magnetic decantation (B_0 = 0.5 T), after which the black precipitate was washed five times with an aqueous solution of nitric acid (200 ml, 1 M). Finally, the particles were dispersed in deionized water, sonicated (45 minutes), and centrifuged (16 500 g; 45 min) to remove aggregates.

The as-obtained NP suspension (20 ml; [Fe] = 250 mM) was diluted with DMF (50 ml) and water was eliminated under reduced pressure. TEPSA (25 mmol; 7.1 ml) was then slowly added to the nanoparticle dispersion in DMF; water was then added (4.3 ml), followed by an aqueous solution of TMAOH (1 M; 2.5 mmol; 2.5 ml) at room temperature and under stirring. The solution was heated to 100 °C for 24 h under continuous stirring. The magnetic nano-objects were collected after pouring the suspension in an acetone–diethylether mixture and magnetic decantation. After washing with acetone, the black precipitate was dispersed in water and purified by membrane filtration (membrane cut-off: 30 kDa) and finally centrifuged (16 500 g; 45 minutes). An amount of 3.2 COOH/nm^2 has been estimated from TGA analysis.

ZW800 derivatization

The NIR-dye preparation has been slightly adapted from an existing protocol, which allowed us to introduce the desired amino function.[32] To do so, 3-(4-hydroxyphenyl)propionic acid (1 g; 6 mmol) was firstly modified through the introduction of *N*-boc-1,4-butanediamine moiety (1.15 mL; 6 mmol) in THF (10 mL) with EDC (1.26 g; 6.6 mmol) as the coupling agent. After 12 hours at room temperature, the solvent was eliminated under reduced pressure, and the resulting residue was purified by flash chromatography (mobile phase: dichloromethane/MeOH 95/5), affording the expected linker. In a second step, the modified phenol (750 mg; 2.2 mmol) was heated with chlorinated dye (634 mg; 0.8 mmol) in DMSO (15 mL) in the presence of diisopropylethylamine (400 μL; 2.3 mmol) at 65 °C for 6 hours. After cooling, the resulting solution was poured in a mixture of ethanol and ethyl acetate (1/1) containing 0.1% formic acid. The as-obtained residue was diluted in dichloromethane containing 10% trifluoroacetic acid, and stirred for 1 hour at room temperature. Finally, the product was isolated after evaporation of the solvents under reduced pressure followed by several washing steps of the solid using dichloromethane and ethanol. The dark green solid obtained after filtration was used without further purification.

^{1}H NMR (500 MHz, D_2O:CD_3OD, 298 K) δ (ppm): 8.02 (d, J = 13.9 Hz, 2H), 7.82 (d, J = 13.9 Hz, 2H), 7.75 (s, 2H), 7.34 (d, J = 8.4 Hz, 2H), 7.28 (d, J = 8.6 Hz, 2H), 7.03 (d, J = 8.6 Hz, 2H), 6.23 (d, J = 14.0 Hz, 2H), 4.22 (t, J = 7.0 Hz, 4H), 3.54 (m, 4H), 3.16 (s, 18H), 3.03 (t, J = 7.1 Hz, 2H), 2.94 (t, J = 7.5 Hz, 2H), 2.84 (t, J = 7.2 Hz, 2H), 2.74 (m, 4H), 2.48 (t, J = 7.4 Hz, 2H), 2.28 (p, J = 7.9 Hz, 4H), 2.01 (t, J = 5.2 Hz, 2H), 1.61 (m, J = 8.0 Hz, 2H), 1.49 (m, J = 7.4 Hz, 2H), 1.33 (s, 12H).

HRMS (ESI+) calculated for $C_{55}H_{77}N_6O_8S_2$ m/z 1013.53, found $[M]^{2+}$: m/z 507.

Vis/NIR in PBS; λ_{max} = 761 nm.

Synthesis of ZW800-labeled SPIO-5

A small amount of trifluoroacetate salt (8 μmol; 9 mg) was added to an aqueous dispersion of TEPSA-modified nanoparticles ([Fe] = 100 mM; 15 ml) in the presence of *N*-(3-dimethylaminopropyl)-*N*′-ethylcarbodiimide hydrochloride (300 μmol; 57 mg) as a coupling agent at pH 7.5. After one night under stirring, the ferrofluid was purified by membrane filtration (membrane cut-off = 30 kDa) and centrifuged (16 500 g; 40 minutes). The resulting suspension was divided into three equal parts (5 mL), each of them being treated with a *O*-(2-aminoethyl)-*O*′-methylpolyethyleneglycol derivative (80 μmol) and EDC (100 μmol; 19,1 mg). The pH was then adjusted to 6.5 and the mixture was stirred at room temperature. After 15 hours of reaction, the suspension was purified by dialysis (membrane cut-off: 12–14 kDa), followed by membrane filtration (membrane cut-off = 30 kDa) until no fluorescence could be detected in the supernatant.

Small animal *in vivo* imaging

Mouse strains and housing conditions. Female 6 weeks old CD1 mice (for MRI) and female 6-week-old hairless SKH1 mice (for FLI and MSOT) were purchased from Charles River (Écully, France) and kept under individually ventilated cage (IVC) housing conditions (12 h/12 h night and day cycles, 22 ± 2 °C, 55 ± 10% relative humidity) and were given dry food and water *ad libitum.* All experiments were performed in accordance with EU Directive 2010/63/EU for animal experiments and were approved by the CEBEA (Comité d'Ethique et du Bien-Être Animal) of the CMMI under approval numbers CMMI-2011-07.

Magnetic resonance imaging. A total of 14 CD1 mice were studied (n = 3 or 4 for each compound and 3 controls). Mice (12–20 weeks) were anesthetized with isoflurane vaporized in oxygen and placed in a cradle adapted for mouse body imaging. Animal temperature was maintained by warm water circulating in a blanket during the whole anaesthesia period, and the respiratory rate was monitored. Mice were intravenously injected with SPIO (70 micromoles Fe kg^{-1}) through a catheter (30 G needle) placed in the tail vein. MRI was performed with a Bruker Biospec 9.4T scanner (Karlsruhe, Germany), using a 40 mm volume coil. Signal enhancement was dynamically observed on T_1-weighted acquisitions with 1 min time resolution (FISP sequence: TR = 4.4 ms, TE = 1.5 ms, flip angle = 15°, NEX = 5, resolution = 125 × 125 × 1000 micrometers). A series of 20 images was acquired and SPIO-5 were injected during the 5th image, allowing for a 16 min analysis. Another FISP image was acquired 1 h after injection. Signal enhancement in blood was measured by ROI drawing in the largest heart chamber seen on the image (ventricle) and expressed as a percentage relative to a mean signal intensity value calculated from the 4 pre-contrast acquisitions. Signal enhancement in the vena cava was illustrated using a RARE sequence (TR = 389.1 ms, TE = 8.1 ms, NEX = 6, resolution = 129 × 141 micrometers, slice thickness = 1 mm). Signal darkening induced by SPIO-5 accumulation in the liver was visualized with RARE sequence (TR = 2000 ms, TE = 17 ms, NEX = 5, resolution = 129 × 121 micrometers, slice thickness = 1 mm, RARE factor = 4). Kidney elimination of SPIO-5 was monitored with MSME (Multi-Slice-Multi-Echo) T_2-weighted sequence (TR = 2000 ms, TE = 7.5–181 ms (24 echoes), NEX = 2, resolution = 344 × 352 micrometers, slice thickness = 1 mm). Liver signal darkening and T_2 of renal pelvis were measured by ROI drawing in Paravision 5.1 software (Bruker, Karlsruhe, Germany). Data were expressed as a percentage referring to the signal intensity or T_2 collected on the pre-contrast image.

Fluorescence imaging. Hairless female SKH1 mice were anaesthetized using isoflurane (4% for induction and then 2% for mouse imaging) vaporized in 100% oxygen at 0,3 L min^{-1}; N = 3 for each group. The mice were then placed on a preparation pad, and a catheter (home-made with 30 G needle) was placed in the tail vein and fixed in place using tissue glue. Images were acquired with a PhotonIMAGER Optima (Biospace Lab, France) equipped with a 4-views module, which allows the simultaneous acquisition of the back, the belly and both flanks, and a homogenous excitation from 3 angles around the mouse body. 25 nm bandpass filters were set, centered on 737 and 797 nm for excitation and emission respectively. Images were acquired before and after 1, 2, 3, 4, 5, 10, 15, 20, 25, 30, 45, 60, and 90 min, and 1, 2, 3, 4, 7, and 14 days injection of SPIO-5 (70 μmol kg^{-1} mouse in saline at 10 mM). The fluorescent signal was measured after drawing ROIs on the mouse in the area surrounding the analyzed organs (liver, right kidney, bladder and thorax) using M3Vision software (Biospace Lab). It was exported and expressed as photons per second per square centimeter per steradian (ph/s/cm^2/sr). The signal was measured on pre- and post-injection images and the ratio "signal injected"Signal non-injected" was calculated to show the signal evolution.

Optoacoustic imaging. A commercial MSOT system (inVision 256-TF; iThera Medical GmbH, Germany) was used for this study. Briefly, a tunable Nd:YAG laser provides 9 ns excitation pulses at a repetition rate of 10 Hz, and it covers wavelengths ranging from 660 to 1300 nm. The peak pulse energy is 90 mJ at 720 nm. Ten optical fibers provide 360° uniform illumination of the mouse. Ultrasound is detected by 256 toroidally focused ultrasound transducers with a center frequency of 5 MHz that are organized in a concave array of 270-degree angular coverage.

Hairless female SKH1 mice were anaesthetized using isoflurane (4% for induction and then 2% for mouse imaging) vaporized in 100% oxygen at 0,3 L min^{-1}; N = 3 for each group. The mice were then placed on a preparation pad, and a catheter (home-made with 30 G needle) was placed in the tail vein and fixed in place using tissue glue. The mice were subsequently

moved into a custom animal holder (iThera Medical) wrapped in a thin polyethylene membrane, with ultrasound gel (Aquasonic Clear; Parker Labs) used to couple the skin to the membrane. The holder was placed within the imaging chamber of the MSOT system filled with water maintained at 34 °C, with the end of the catheter line available outside of the imaging chamber for contrast agent injection. The mice were allowed to stabilize their physiology for 10 minutes within the system prior to initialization of the scan. Images were acquired using 8 wavelengths (675, 700, 725, 755, 775, 800, 850 and 900 nm) and an average of 10 pulses. The whole abdomen (5 cm) was scanned by 2 mm continuous steps for a scan time of ± 4 min. After 12 min of continuous imaging to establish the baseline signal (*i.e.* 3 runs achieved), a bolus of SPIO-5 (70 μmol kg^{-1} mouse in saline at 10 mM) was injected intravenously through the catheter, followed by a pulse of saline to flush the line, during the 4th run. OT was continued for a further 90 min of continuous scanning. Images were reconstructed using a Model Linear algorithm using viewMSOT 3.8 software (iThera Medical). Fluence correction was performed using a diffusion approximation method (O_2 85%; μa@800 nm 0.22; μs 10.0; water 50%; Fat 30%) in pLabs (iThera Medical). Finally, an AMP spectral unmixing was performed using images of the third run as baseline. ROI were drawn around studied organs (right kidney, pelvis, liver and bladder) and the mean MSOT signal intensity (arbitrary unit) was measured. Then the ratio "signal injected"/"Signal non-injected" was calculated to show the signal evolution.

Mice sacrifice and plasma collection. Mice were sacrificed by lethal injection of ketamine/xylazine (according to the project no 2011-07 accepted by the ethics committee of CMMI (LA1500589)). During this process, retro-orbital blood collection was performed at the deep anesthesia stage and samples were centrifuged for 10 min. At least 250 μl of plasma had to be obtained for dosage of several toxicity markers using Spotchem EZ Sp-4430 (Arkay®) colorimeter. "Panel-1" and "Kidney-2" strip sets were used and one relevant marker of each was considered to identify possible liver (with glutamate oxaloacetate transaminase (GOT)) and kidney (with blood urea nitrogen (BUN)) damage, as a preliminary (due to a limited amount of mice) assessment. Measurements of glutamate pyruvate transaminase (GPT) and creatinine concentrations, probably better representative of liver and kidney damage, respectively, were also allowed by the strip sets but, in some cases, the blood levels of those markers were too low to obtain a value from the colorimeter. BUN and GOT were thus selected to compare "full" datasets (meaning one value measured above the detection limit of the colorimeter for each studied mouse). CD1 mice and hairless SKH mice were sacrificed 5 months and 2 weeks after SPIO-5 injection, respectively.

Results and discussion

Synthesis and characterization of PEGylated fluorescent SPIO-5

As depicted in Fig. 1, SPIO-5 has been prepared towards a five-step procedure which could be summarized as follows:

- synthesis and surface modification of SPIO (steps 1 and 2)
- size selection process (step 3)
- grafting of NIR-emitting derivative onto the modified surface (step 4) followed by PEGylation (step 5)

Because of its effectiveness to produce large amounts of highly concentrated and relatively poorly dispersed nanostructures, we chose to prepare the oxide cores by the co-precipitation of iron salts in diethylene glycol.[33,34] As previously described,[35,36] the particle's surface has been modified by means of organosilane treatment (*i.e.* 3-(triethoxysilyl)propyl-succinic anhydride (TEPSA)), which resulted in the introduction of the desired carboxylic functions. The advantage of this method lies in the stability of the deposited coating (formation of a stable Fe–O–Si covalent bond) and in the relative control of the layer thickness that appears as very thin as indicated by PCS (16.4 nm for bare NPs and 18.8 nm for TEPSA-coated NPs; Fig. S1, ESI†). One may note that no enlargement of the size distribution was observed following the silanization step, suggesting the coating of individual objects.

Owing to their potential applications in T_1-weighted vascular imaging, or as passive tumor targeting agents, our study is focused on 5 nm SPIO. To isolate the fraction of interest, a magnetic size sorting procedure (*i.e.* magnetofiltration (MF)), was adapted from a previously[37] described protocol. This sorting process was performed by using columns filled with ferromagnetic beads; the separation being essentially gravitational (*i.e.* no elution flow control was applied). When the column is placed in a magnet, the beads create strong magnetic field gradients retaining magnetic particles according to their global magnetic moments,[34] and, consequently, to their sizes. SPIO-5 have been isolated from the initial suspension ([Fe] = 200 mM) by sorting the first elution fraction escaping from a primary magnetic treatment (0.5 T), and by submitting it in a next step to a stronger magnetic field (0.9 T). By proceeding this way, we were able to progressively separate the bigger nanoparticles from the smaller ones without saturating the column. The efficiency of the process has been assessed by relaxometry (Table 1), and more specifically through the comparison of the NMRD data (Table 1), for which significant differences can be noticed between the recorded profiles (Fig. 2), reflecting the evolution of the particle size distribution towards small particle diameters. Although more subtle (especially between TEPSA-0.5T and TEPSA 0.9T), this evolution towards smaller sizes was also observed by PCS (Fig. 2), and further confirmed by TEM (Fig. 3), where an evolution of the mean size from 7.5 ± 2.6 nm to 4.9 ± 0.9 nm has been noticed following the proposed treatment. Overall, such a size sorting process appeared to be very efficient for the isolation of the desired SPIO-5, by providing nearly monodisperse SPIO-5 (PDI = 1.14 *vs.* 1.48 before magnetic filtration) in a relatively high yield (approx. 35% regarding the iron concentration of the initial ferrofluid).

Optical properties have been obtained through the introduction of a NIR-emitting derivative (namely, a ZW800-1 analogue[32]) for which structure (Fig. 1) and preparation have been slightly adapted in order to introduce the requested end-amino function. The as-synthesized derivative has been covalently grafted onto the surface towards the use of EDC as

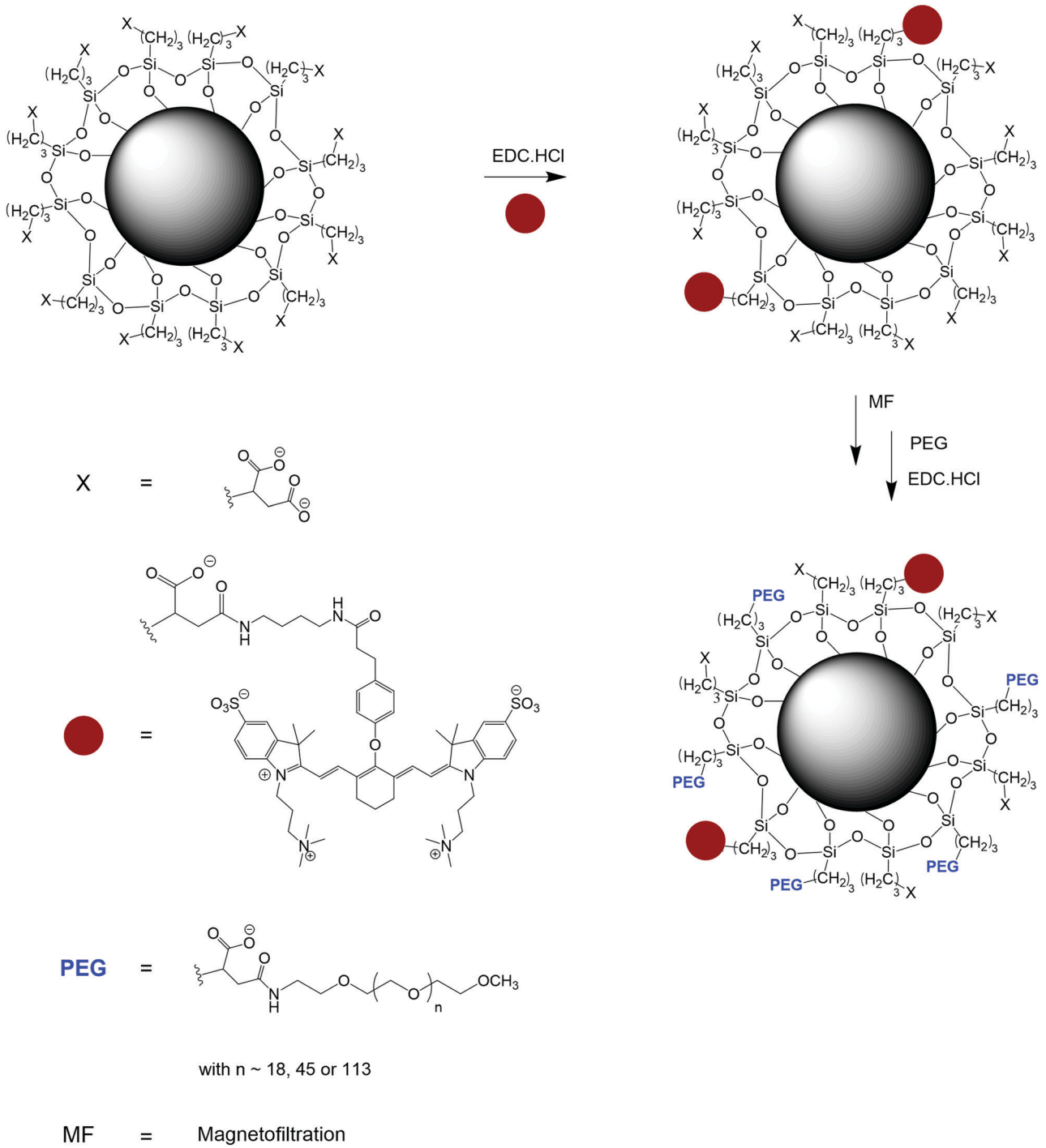

Fig. 1 Schematic illustration of the synthetic procedure applied to obtain the proposed bimodal SPIO-5.

a coupling agent. The resulting suspension has been purified from ungrafted dyes by mean of dialysis and membrane filtrations till the total disappearance of any emission signal in the supernatant. At this stage, the resulting suspension has been divided into three equal aliquots, each of them being treated with α-amino,ω-methoxy-PEG of various molecular weight, *i.e.* 800 Da (PEG-800), 2 kDa (PEG-2k) and 5 kDa (PEG-5k). PEG chains were introduced onto the surface by treating the suspension with an excess of polymer in the presence of EDC. PCS measurements (Table 1 and Fig. S2, ESI†) suggest the introduction of the polymeric chains onto the surface by displaying an increase of 5, 7.8 and 19.5 nm respectively for SPIO-5-800, SPIO-5-2k and SPIO-5-5k in comparison with TEPSA-stabilized particles. No differences in the core size were noticed by TEM (Fig. S3, ESI†). The comparison of the relaxometric data collected for the different batches of SPIO-5 are

Table 1 Summary of the physicochemical data obtained for the different SPIO

Sample	Zeta potential (mV) (25 °C; pH 7)	Relaxometric properties (20 MHz; 37 °C)			Diameter		NMRD data	
		r_1 (s^{-1} mM^{-1})	r_2 (s^{-1} mM^{-1})	r_2/r_1	D_{PCS} (nm)	D_{TEM} (nm)	D_{NMRD} (nm)	M_s^{NMRD} (A m^2 kg^{-1})
TEPSA-raw	−40.4	32.34	73.04	2.26	21.03	7.5 ± 2.6	10.54	51
TEPSA-0.5T	−39.1	25.28	44.65	1.77	13.55	7.0 ± 1.9	8.28	53.6
TEPSA-0.9T	−44.8	19.73	32.03	1.62	13.21	4.9 ± 0.9	6.80	56.1
SPIO-5-800	−0.02	19.85	32.18	1.62	18.17	4.8 ± 1.0	6.92	55.9
SPIO-5-2000	−7.8	20.07	32.79	1.63	21.04	4.8 ± 0.9	6.78	57.1
SPIO-5-5000	−13.4	19.90	32.81	1.65	32.67	5.0 ± 1.0	7.12	55.6

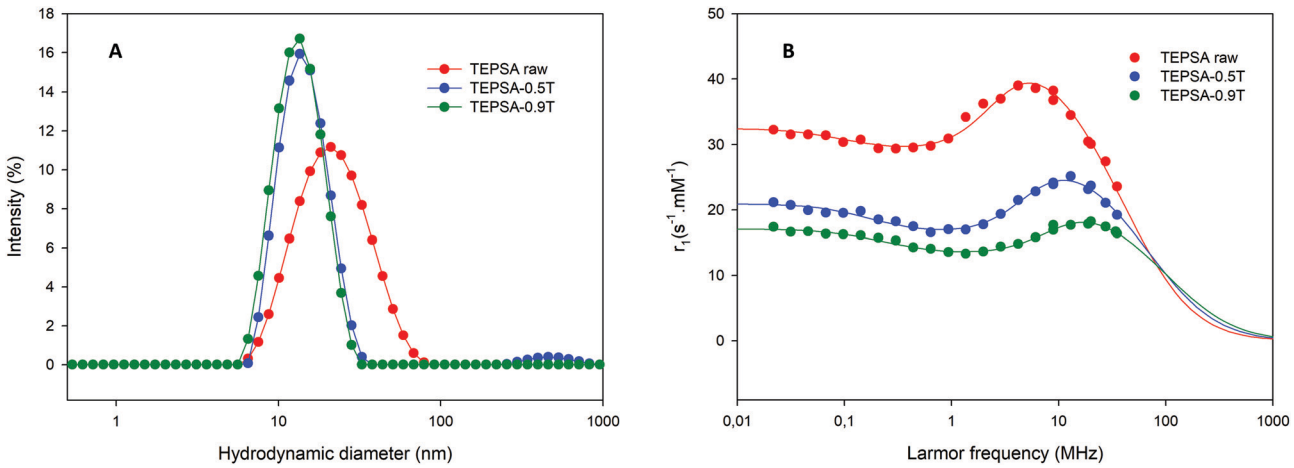

Fig. 2 Comparison of the hydrodynamic size distributions (left) and of the NMRD profiles (right) of TEPSA-modified SPIO following different steps of the magnetic sorting procedure.

summarized in Table 1 and Fig. S4 (ESI†). Surprisingly, no significant difference could be observed between the different PEGylated particles. Indeed, according to the "outer-sphere" theory, one may suppose a decrease of the relaxivities when increasing the coating thickness. An explanation for these unexpected values may arise from the differences observed in the grafting densities between the samples (*i.e.* the density increases when decreasing the PEG molecular weight; Fig. S5, ESI†). More specifically, the number of PEG chains grafted to the SPIO nanoparticles decreased by 3-fold from 184 for mPEG800 (2.4 PEG nm^{-2}) to 37 for mPEG5k (0.5 PEG nm^{-2}) (a density of 0.63 PEG nm^{-2} being determined for mPEG2k). This result is supported by the zeta potential measurements, for which a decrease upon negative values was observed when increasing the PEG length (Table 1).

The Flory radius (F) defined as:

$$F = \alpha n^{3/5} \quad (1)$$

where n is the number of monomers per polymer chain and α is the length of one monomer (3.5 Å for PEG)[38,39] provides information about the two main conformations that PEG chains can acquire depending on grafting density (*i.e.* "mushroom" and "brush"). Typically, a "mushroom" conformation is observed for low surface densities when the distance (D) between the attachment points of a polymer to a surface is larger than F ($D > F$), D being defined as:

$$D = \frac{\sqrt{4\pi r^2}}{N} \quad (2)$$

where r is the NP radius and N is the number of molecules grafted.

On the contrary, a "brush" conformation is observed for $D < F$. Whatever the chain length, none of the values of D were found to be greater than F. Similarly to other reports,[39] we can assess that in the present work the "brush" conformation is the exclusive conformation, despite the fact that grafting density was found to decrease with the PEG chain length. As the relaxivity values depend on the ability of the water molecule to reach the iron oxide surface where the field lines of the magnetic moment are strong, one may suppose that the increase of the hydrodynamic diameter with increasing chain length is compensated by the ability of water molecules to easily diffuse through the polymeric network.

After purification, the resulting ferrofluids exhibited strong emission signal around 790 nm after excitation at 750 nm. Emission signal intensity increased proportionally from 0.1 mM to 1 mM Fe, which was the maximum concentration evaluated (Fig. S6, ESI†). Assuming that iron oxide cores are monodisperse and spherical, an approximative amount of 1 dye per particle has been estimated. When comparing to the estimated amount of carboxylated functions introduced onto

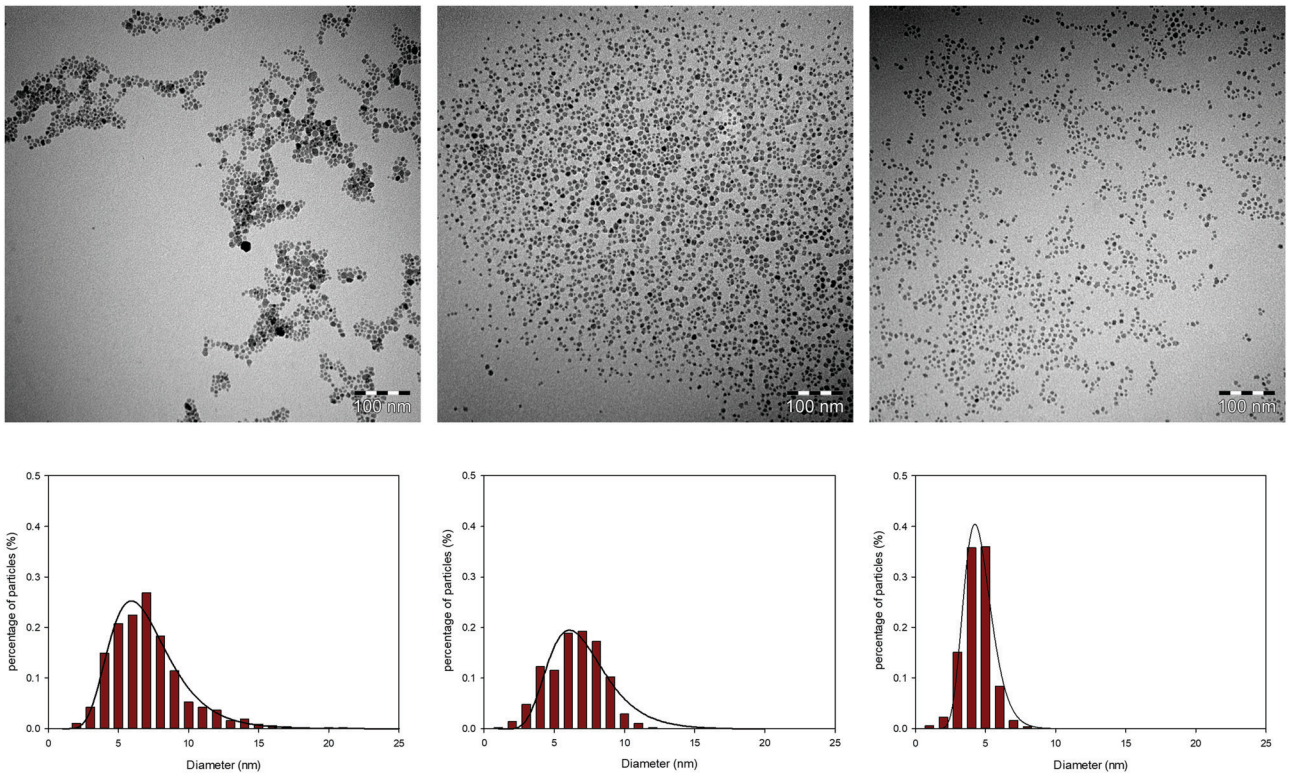

Fig. 3 Comparison of the TEM images (scale bar: 100 nm) and size distributions determined by TEM (scale bar: 100 nm) of TEPSA-modified SPIO before (left) and after the magnetic sorting procedure at 0.5T (middle) and at 0.9T (right).

the surface, a grafting yield around 0.5% was determined. Such value may appear low but, in practice, was sufficient to get a strong signal in FLI and MSOT. Indeed, *in vitro* fluorescence measurements using the *in vivo* imager showed a strong NIR emission which was detectable from the concentration of 100 μM of iron. For a given concentration in iron, no significant difference in the emission signal could be noticed between all the samples. The signal reaching a maximum intensity plateau at 1 mM, started to decrease at 5 mM probably due to decreased light penetration into the darker solution, or quenching (Fig. S6, ESI†). As shown in Fig. S7 (ESI†), the resulting SPIO-5 were also generating a strong photoacoustic signal. SPIOs exhibited very similar optoacoustic spectra, with a maximum signal intensity at a wavelength of 775–780 nm. Indeed, they were detectable since 100 μM Fe to 5 mM Fe. Above this concentration, the signal drifted to 790–800 nm and the shape spectra gets flatter, suggesting that the concentration was too high because of light quenching (results not shown). Finally, a significant enhancement of the signal intensity in the presence of the particles has been observed for all the samples at 9.4T. The evidence of this T_1 effect observed at such a high field (*i.e.* 400 MHz) indicates the high stability of the presented systems. As expected, a strong T_2 effect has also been highlighted (Fig. S8, ESI†).

Small animal *in vivo* experiments

Blood/heart examination. FISP MRI sequences (20 repetitions of one minute each) were applied to dynamically follow the evolution of the signal in the left cardiac ventricle over time after the injection of the different SPIO-5. As depicted in Fig. 4, a strong increase of the signal was observed 2 minutes post-injection for all the samples. Interestingly, while the ventricular blood signal of the mice injected with the SPIO-5-800 is already strongly attenuated 4 hours post-injection, it remains increased at 7 hours after injection in those that received SPIO-5-2k and SPIO-5-5k, indicating that these particles maintain a higher concentration in circulation for a longer time period regarding SPIO-5–800. The day after the manipulation (D1), the heart ventricle returned to a signal similar to the pre-injection situation. Measurements performed on mice's thorax by FLI (Fig. 5), which is reflecting blood circulating SPIO-5, showed that there is persistence of both SPIO-5 to 7–14 days after injection. SPIO-5-2k and SPIO-5-5k showed very similar kinetics, except at 1 and 2 days in which SPIO-5-2000 showed a more intense signal. SPIO-5-800 showed a stronger signal intensity in the first min following injection, but then a faster washout which led to a weaker signal after 45 min.

Overall, these results indicate that the molecular weight of the PEG grafted onto the SPIO surface significantly influences the rate of signal recovery in the vascular compartment, and therefore the SPIO elimination rate. It is difficult to correlate this behavior to the respective SPIO-5 properties. One may suggest that smaller PEG chains may give lower stealthiness regarding longer chains. This hypothesis may correlate with the observation reported by Weller[14] who observed that the molecular weight of the PEG grafted onto 4 nm particles may have significant impact upon *in vitro* phagocytosis. In addition,

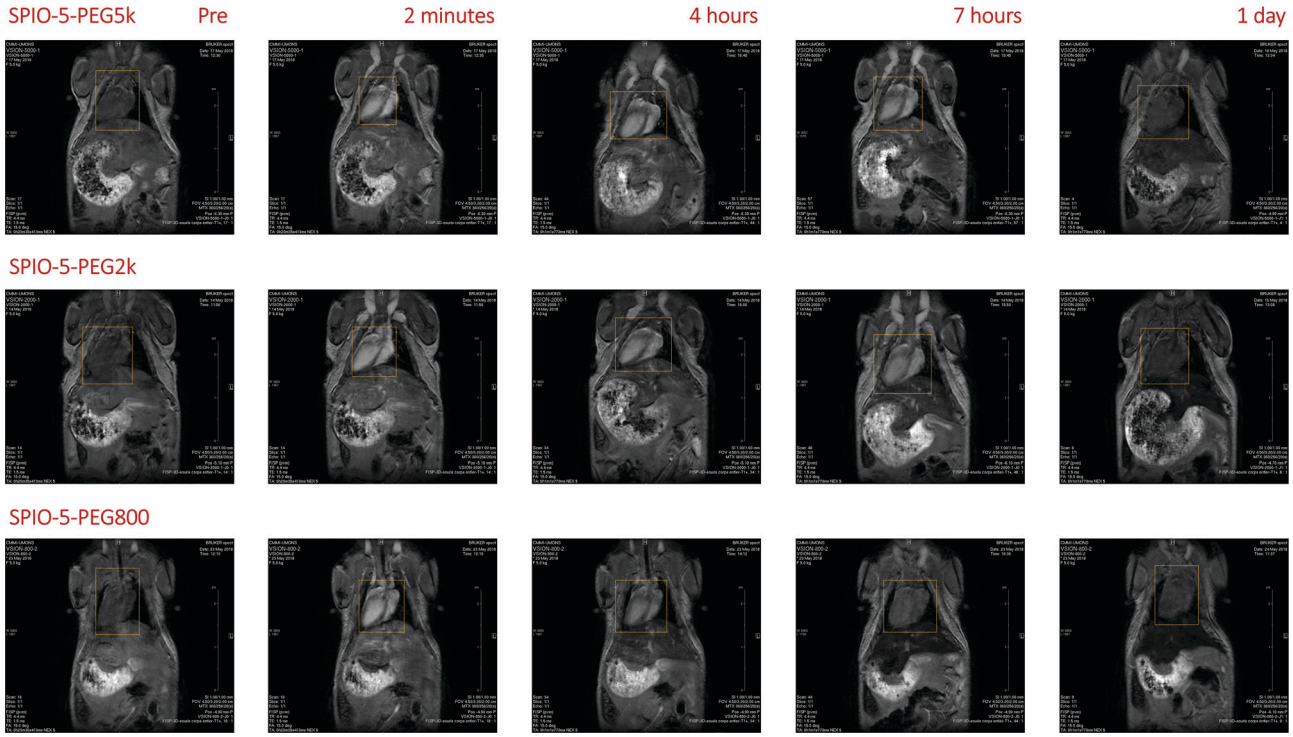

Fig. 4 Illustration of *in vivo* MRI data collected on mice treated with the different types of SPIO-5 at a dose of 70 μmol Fe kg^{-1}. Positive signal enhancement in T_1-weighted FISP imaging before, at maximum contrast (2 min), after 2 h, after 4 h and one day after injection. The yellow square indicates the area in which signal intensity measurements were performed.

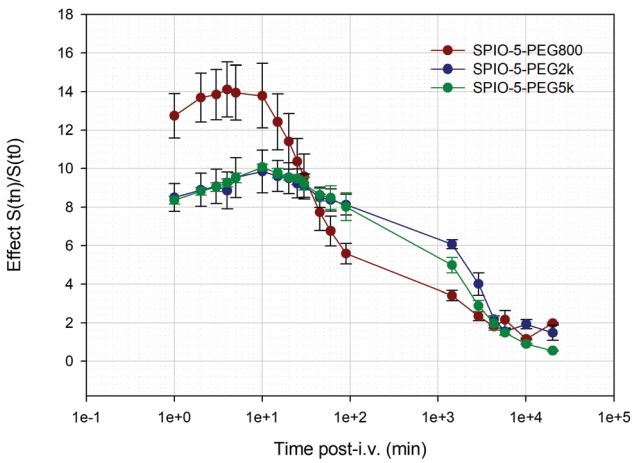

Fig. 5 Evolution of the FLI signal (as expressed as the ratio of the signal at each timepoint over the signal before injection) over time in the thorax of mice injected with the different types of SPIO-5.

protein corona (both hard and soft) formed on nanoparticles upon their injection in the blood stream can strongly influence their behavior *in vivo*, more particularly, the interaction with platelets and blood cells, which in turn influences removal of the particles from blood.[40] As an example, it has been recently reported that the adsorption of apolipoprotein E (ApoE) appeared to be dependent on PEG density.[38] For this protein, nanoparticles with higher PEG densities appear to have a lower relative abundance of ApoE. From our side, the follow-up by PCS of the different SPIO-5 batches incubated with a solution of HSA (0.5 mg mL^{-1}) suggests some subtle differences between the batches. So, for SPIO-5-800 if no increase of the mean size distribution could be observed, the very quick appearance of a second population was noticed (within minutes) (Fig. S9, ESI†). Interestingly, it took between 2 and 4 hours to make a similar observation for SPIO-5-2k, while such behaviour was not observed for SPIO-5-5k, even after 8 hours incubation. Taken together, these results suggest a potential influence of the protein corona on the circulation times observed for the studied nanosystems. Finally, differences in the hydrodynamic size of SPIO covered with different PEG chains can also influence their clearance, as suggested by the subsequent results.

Liver examination. MR images of the liver were performed using a T_2-weighted RARE sequence. Similarly to the observations made in the vascular compartment, the evolution of the signal over time shows strong differences in the capture and residence time of SPIO-5 in the liver, such behavior depending on the PEG molecular weight. Early after injection (36 minutes), the T_2 effect induced by SPIO-5-800 induced a significantly greater liver signal decrease than other SPIO-5 (−62% *vs.* −40%; Fig. 6). This behavior reflects a slower liver uptake that may be expected from SPIO-5-2000 and SPIO-5-5000 and suggests a reduced adsorption of opsonins on nanoparticles with longer PEG chains. After reaching a minimum at day 1 (around −80%), the signal progressively increased until reaching a maximum of −32%, 12 weeks post-injection. No more evolution of the signal was observed after this period.

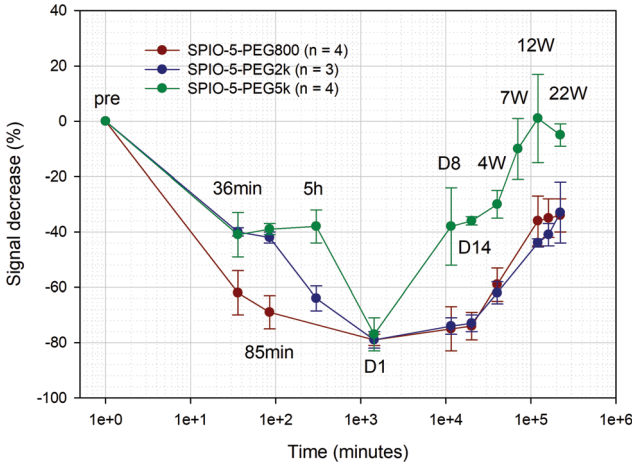

Fig. 6 Evolution of liver signal after injection of SPIO-5-800, SPIO-5-2000 or SPIO-5-5000, at 36 min, 85 min, 5 h, day 1, day 8, day 14, 4 weeks, 7 weeks, 12 weeks and 22 weeks.

SPIO-5-2k were also fairly quickly taken up by the liver. However, it took 5 h to observe a signal decrease as strong as the drop observed for SPIO-5-800 at 36 min. Before this drop, the signal remained significantly less attenuated and appeared fairly stable (−40% after 36 min and −43% after 85 min). A minimum of −76% was observed one day after injection. Then, the signal gradually increased and reached a maximum of −31% at 22 weeks *post*-injection.

The curve obtained with the SPIO-5-5k showed a hepatic signal decrease up to – 41% from 36 min post-injection, but it remained stable and significantly less attenuated than other SPIO-5, up to 5 hours after injection. This observation highlights a slower uptake for particles coated with a PEG5k, suggesting a slower opsonization for high molecular weight PEG-coated SPIO. This weaker capture seems to be related to an increased stealth for these particles and is consistent with the extended circulation times observed with SPIO-5-5k. Similarly to the other particles, the hepatic darkening is the strongest on day 1 post-injection, reaching around – 80% of signal decrease. Interestingly, a faster signal recovery has been observed for these particles. A liver signal similar to that observed at 4 weeks with SPIO-5-5k was only observed 8 weeks later for the other types of SPIO-5 (and was actually their maximum signal recovery). Noticing this tendency at previous time points, an additional observation was thus added at 7 weeks for SPIO-5-5k in order to more precisely follow liver signal increase, allowing us to determine that, on the contrary to the observations made for SPIO-5-800 and SPIO-5-2k, a total signal recovery has been reached between 7 and 12 weeks post-injection for SPIO-5-5k.

It is not totally clear why such a "signal stagnation" phenomenon occurred with SPIO-5-800, but it may result from combined effects of the remaining SPIO-5 in liver cells, for which complete degradation was not achieved, and of natural increase of iron content in the liver with age (mice were indeed aged between 10 and 11 months at the end of the MRI study). It was indeed reported that the liver iron content of aged mice (16–19 months) significantly increased compared to that of young adults (2–6 months), especially in females of several mouse strains.[41] Despite the fact that this study did not include CD1 mice and did not explore animals aged between 6 and 16 months (which is the range in which the age of our CD1 mice is situated at the end of the MRI study), it is nevertheless a clue supporting the fact that the liver may have an additional source of signal decrease, possibly masking its recovery from SPIO-5-induced darkening. Furthermore, at 22 weeks, on the one hand, those injected with SPIO-5-5k showed a liver signal decrease tendency (however not significant) from their apparent "total recovery" state, maybe related to a natural increase of liver iron content with age. On the other hand, those injected with SPIO-5-2k showed a signal increase tendency, suggesting that SPIO degradation was still ongoing and that further observations

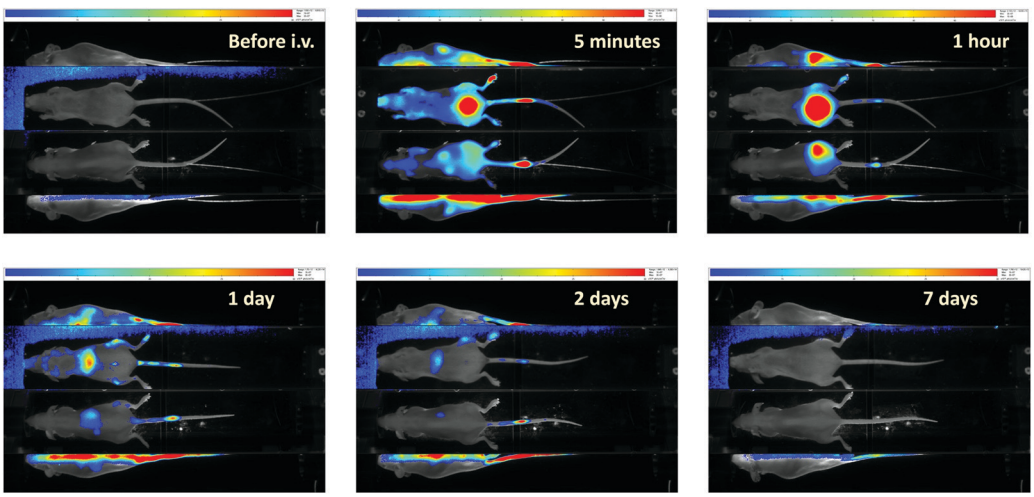

Fig. 7 4-Views FLI of a mouse injected with SPIO-5-800. Intensity scale: Pre-i.v., Day 1, 2 and 7 = 1×10^7 to 3×10^7 ph/s/cm^2/sr; and 5 min and 1 h: 3×10^7 to 1×10^8 ph/s/cm^2/sr. Kidneys are moderately stained at 5 min post-i.v. (dorsal and laterals views), but became invisible at later timepoints. Bladder is already positive from 5 min and strongly positive at 1 h (belly view). After miction at mouse wake-up, bladder staining is not yet visible. Liver accumulation in visible in the belly at 1 and 2 days. At 7 days, emission is no longer visible.

might have confirmed liver signal recovery, or stagnation at about – 30% such as in SPIO-5-800-injected mice.

FLI showed weak liver staining, mostly at 24 h and 48 h and mainly for SPIO-5-800 (Fig. 7). Unfortunately, the strength of the signal coming from blood (as described in the previous chapter) and/or surrounding organs unpair any robust quantitative analysis. Nevertheless, these qualitative observations are correlated to peaks of signal loss measured by MRI. MSOT was not sensitive enough to detect SPIO-5 in the liver probably due to the bad signal to noise ratio generated by this organ. Indeed, the liver is strongly pigmented and is a large organ causing huge light attenuation, and generating a relatively strong background photoacoustic signal because of its high hemoglobin content.

Kidney/bladder examination. In order to complete data concerning the elimination pathways, T_2-weighted images were carried out using MSME sequences and T_2 value of the renal pelvis was measured. Fig. 8 represents the evolution of the renal pelvis T_2 value over time, relative to a pre-injection measurement. It is interesting that, despite significant differences in their hydrodynamic diameter (18.2 nm for SPIO-5-800, 21 nm for SPIO-5-2k and 32.7 nm for SPIO-5-5k), the three types of SPIO-5 showed very similar T_2 decrease 27 min post-injection (−60% for SPIO-5-800, −62% for SPIO-5-2k and −66% for SPIO-5-5k). Marked differences appeared 57 min after injection, where T_2 decrease appeared stronger for SPIO-5 capped with longer PEG chains. This difference continued to increase with time until the total signal recovery after 5 hours for the mice treated with SPIO-5-800. For the mice treated with the other SPIO-5, a strong darkening due to T_2 decrease is still visible in the area of the renal pelvis more than 300 min post-injection. As cardiac ventricle and liver-focused MRI analyses suggested, SPIO-5-800 undergo faster blood clearance due to faster and greater hepatic uptake from circulation, regarding SPIO-5-2k and 5k in the first hours post-injection. Only with SPIO-5-800, significant re-increase of T_2 in the pelvis is happening during this early observation period. It is probably a consequence of the faster and greater hepatic uptake of SPIO-5-800, which quickly decreases their availability for renal filtration from blood circulation. Renal filtration thus appears to occur for each SPIO-5 type but can be depicted in the MRI at times where there is a sufficient remaining amount of SPIO-5 in circulation. Hydrodynamic diameter increase due to increasing PEG size may have introduced the influence of the mechanical limitations of renal filtration on the results, but it was not observable in our MRI conditions. One day after injection, the signal returned to its initial state for all the SPIO-5, even if a non-complete recovery seemed still visible for some mice treated with SPIO-5-5k.

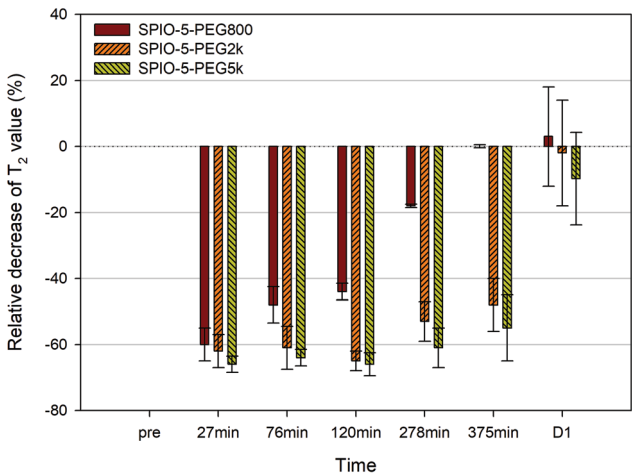

Fig. 8 T_2 decrease (%) in the renal pelvis of mice at different times after injection of SPIO-5-800, SPIO-5-2k or SPIO-5-5k.

These observations are consistent with the observation made by MSOT (Fig. 9). In MSOT experiments, signal intensities were measured in the right kidney's pelvis. All SPIO-5 showed a signal intensity peak a few minutes after injection, but SPIO-5-800 showed the strongest and narrowest. They both came back to their basal level after 90 min. In FLI experiments, the signal is not specific enough to reflect the SPIO-5 filtered by kidneys. As the signal is measured on the skin (surface measurement), it is made of an overall mixture of filtrated SPIO by the kidney, of SPIO located in the blood stream inside the kidney, but also in the surrounding tissue such as the skin. Nevertheless, kidney clearance was shown qualitatively because of the kidney's staining. On the contrary, the signal is precisely measured in the kidney's pelvis using MSOT because of its tomographic approach with high spatial resolution. Consequently, the measurement in MSOT is far more precise and reflects only the fraction of SPIO that was filtered by the kidneys.

FLI analysis of the bladder (Fig. 10) was performed by calculating the ratio between the effect on the signal in the bladder and the effect on the signal in the thorax, to exclude the fraction of signal coming from the blood stream. The evolution of the emission signal over time showed a similar increase for all the samples during the first minutes, followed by a significantly higher signal after 10 minutes for the mice treated with SPIO-5-800. A similar evolution can be observed for the mice treated with SPIO-5-2k and SPIO-5-5k. The signal of the bladder at late timepoints is similar for all SPIO-5 and appears as far weaker, progressively reaching the basal level at day 4. Similar trends can be highlighted by MSOT as depicted in Fig. 10. However, the signal coming from SPIO-5-2k is close to the signal of SPIO-5-800, while the signal coming from SPIO-5-5k is weaker.

Evolution of hepatic and kidney damage markers. Interestingly, BUN concentrations did not reveal any difference between 5 month and 2 week delays. These values remained also similar to the BUN concentration measured on the controls, suggesting that no significant kidney damage was induced by SPIO-5 (Fig. 11). Indeed, an increase of blood urea concentration regarding controls would have been suggestive of kidney failure probably due to the injected compounds. However, colorimetric assessment of BUN concentration, in the limits of what this test allows us to conclude, did not reveal any loss of renal function due to SPIO-5.

GOT, also known as aspartate aminotransferase, is not exclusively representative of the liver. Indeed, this enzyme is

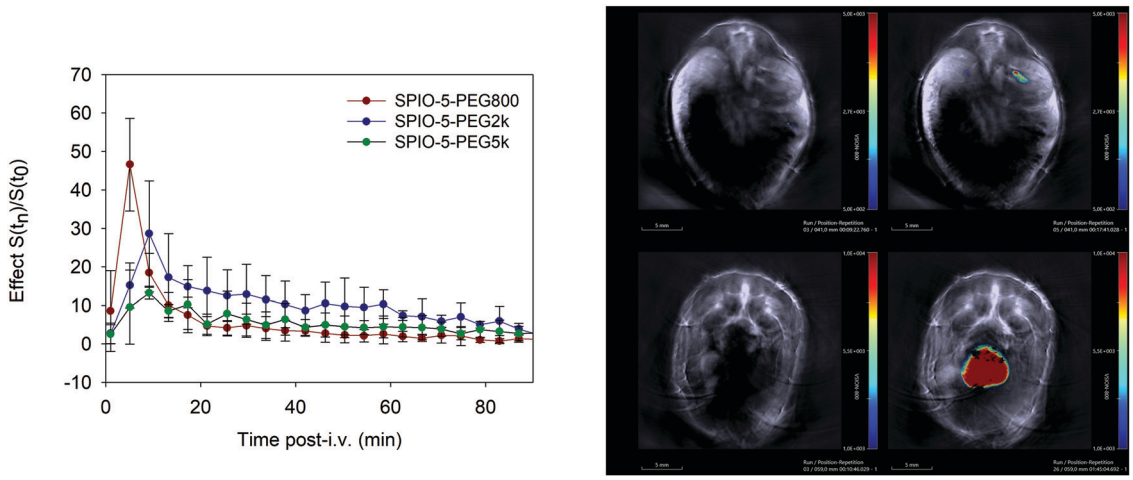

Fig. 9 (left) Evolution of the MSOT signal over time in the kidney's pelvis of mice injected with the different types of SPIO-5; (right) mouse injected with SPIO-5-800 as an example of a typical MSOT scan. 2 slices were analyzed: one through the right kidney (up) and the second through the bladder (down).

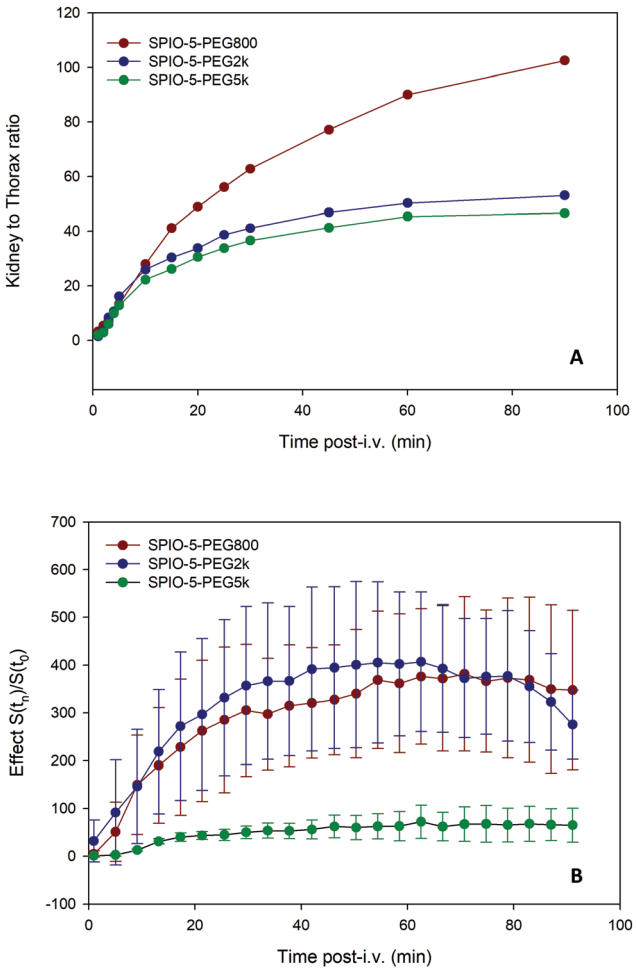

Fig. 10 Evolution of the FLI signal (up) and MSOT signal (down) over time in the bladder of mice injected with the different types of SPIO-5.

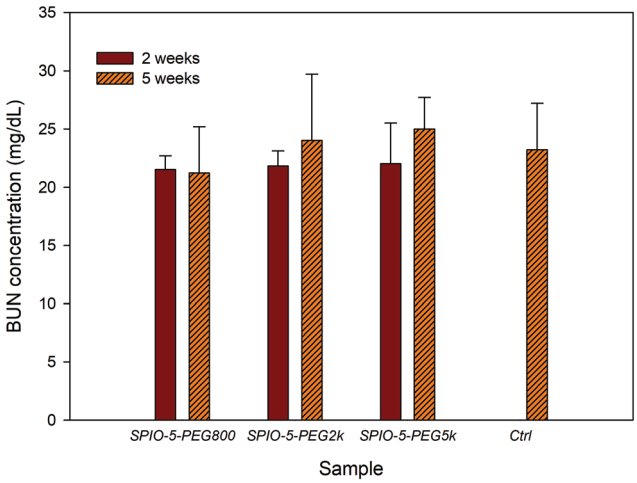

Fig. 11 Blood urea nitrogen (BUN) mean levels in plasma of mice, 2 weeks after injection of SPIO-5-800 (n = 3), SPIO-5-2000 (n = 3), SPIO-5-5000 (n = 3), or 5 months after injection of SPIO-5-800 (n = 3), SPIO-5-2000 (n = 2), and SPIO-5-5000 (n = 3), compared to control mice (n = 3).

also present in muscle tissue (including heart cells) and other organs such as kidneys and pancreas.[42] In case cytolysis occurs in these organs (due to damage or disease), GOT is released in the blood. An increase of GOT plasma concentration in the present study would thus be suggestive of cell lysis due to SPIO-5, possibly not only in the liver, but as no evidence of kidney failure could be noticed, hepatic damage may be the main source of GOT release in the blood. Nevertheless, cardiac and/or renal cell death (however not sufficient to induce loss of kidney function) is not to be excluded as a source of GOT in plasma. For SPIO-5-800 and SPIO-5-5k, GOT plasma concentrations were increased regarding controls at the 2 week delay, but not at the 5 month delay (Fig. 12). Important variability in the SPIO-5-800 group did not allow us to show any significance of the increase of GOT plasma concentration. However, less variability in the SPIO-5-5k group allowed us to show significant increase of GOT plasma concentration 2 weeks after injection compared to controls ($p < 0.05$). Only SPIO-5-2k did not induce GOT concentration increase in the plasma at the 2 week delay.

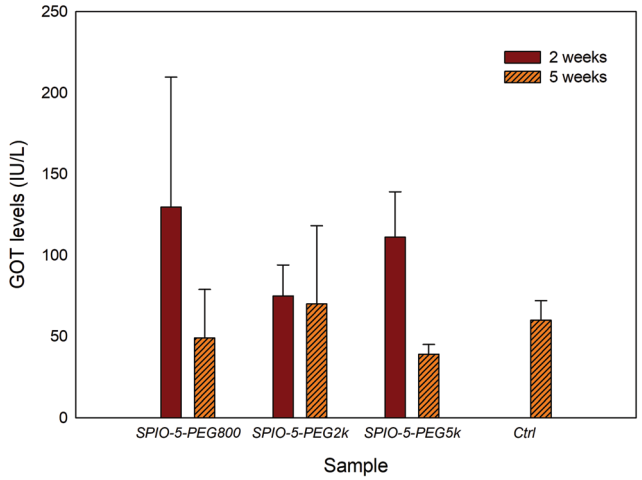

Fig. 12 Aspartate aminotransferase (or glutamate oxaloacetate transaminase (GOT)) mean levels in plasma of mice, 2 weeks after injection of SPIO-5-800 (n = 3), SPIO-5-2000 (n = 3), and SPIO-5-5000 (n = 3), or 5 months after injection of SPIO-5-800 (n = 3), SPIO-5-2000 (n = 2), and SPIO-5-5000 (n = 3), compared to control mice (n = 3).

In the limits of what can be concluded with this test, it may suggest a greater safety of SPIO-5-2k for *in vivo* applications. Maybe the massive and relatively quick uptake of SPIO-5-800 in the liver induces hepatic damage, and the extended circulation time of SPIO-5-5k may allow them to have toxic effects on a longer period regarding SPIO-5-2k. Too thick PEG coating may also be in favor of a more difficult degradation process of SPIO-5-5k by the liver cells and more precisely Kupffer cells, possibly inducing cell death. Nevertheless, at the 5 month delay, GOT plasma concentrations were back to values similar to that of control mice. Furthermore, two additional SKH mice were sacrificed at 3 weeks delay and showed a GOT plasma concentration similar to that of control CD1 mice, suggesting that a recovery from previous cell damage occurred at relatively short term after our 2 week time point, and that those two mice strains probably do not exhibit different basal plasma GOT concentrations (Fig. S10, ESI†).

Conclusions

In this work, the preparation of fluorescent 5 nm iron oxide nanoparticles was demonstrated. SPIO, synthesized by coprecipitation, were submitted to a size-selection process based on magnetofiltration enabling the isolation of the fraction of interest. SPIO-5 were grafted with a NIR-emitting derivative (ZW800-1 analogue) and subsequently treated with α-amino,ω-methoxy-PEG of various molecular weight, *i.e.* 800 Da (PEG-800), 2 kDa (PEG-2k) and 5 kDa (PEG-5k). A complete *in vitro* characterization was performed, showing similar relaxivities for each type of SPIO-5-PEG (evaluated through NMRD profiles and phantom MR images) and similar fluorescent and photoacoustic efficiency. *In vivo* MRI, FLI and MSOT experiments confirmed the significant influence of PEG chain length on the biodistribution profiles of the nanoparticles. We demonstrated longer circulating times for SPIO-5 bearing longer chains of PEG on their surfaces with SPIO-5-2k and SPIO-5-5k showing a persistent increased signal in cardiac left ventricle after seven hours while SPIO-5-800 were washed out after 45 min. Elimination of SPIO-5 by the urinary system (kidneys, bladder) and the liver were confirmed by T_2–w MRI and MSOT experiments, confirming the faster elimination of SPIO-5-800 compared to the other SPIO-5. In this project, MSOT allowed us to monitor fast renal clearance with high sensitivity, and without sacrificing spatial or temporal resolutions.

Finally, follow-up of two plasma markers did not reveal any sign of kidney failure while the liver marker seems to indicate greater safety for SPIO-5-2k. Therefore, we can conclude that SPIO-5-2000 have the best properties among the studied PEG chain lengths, taking advantage of the long circulation time and relatively slow uptake by the liver. These results indicate that SPIO-5 can be a competent probe for T_1–w MRI applications requiring a long imaging window such as clinical MRI angiography.

Conflicts of interest

There are no conflicts to declare.

Acknowledgements

The authors would like to acknowledge the Walloon Region (Gadolymph, Prother-Wal projects), the European Union (NanoCardio project funded by the Interreg France-Wallonie-Vlaanderen program), FNRS, and the COST actions. The Bioprofiling platform, supported by the European Regional Development Fund and the Walloon Region, Belgium, is also acknowledged. Authors thank the Center for Microscopy and Molecular Imaging (CMMI, supported by European Regional Development Fund and Wallonia).

References

1 Y. X. J. Wang and J. Idee, *Quant. Imaging Med. Surg.*, 2017, **7**, 88–122.
2 Z. Shen, A. Wu and X. Chen, *Mol. Pharm.*, 2017, **14**, 1352–1364.
3 N. Lee and T. Hyeon, *Chem. Soc. Rev.*, 2012, **41**, 2575–2589.
4 H. E. Daldrup-Link, *et al.*, *Radiology*, 2017, **284**, 616–629.
5 R. Jin, B. Lin, D. Li and H. Ai, *Curr. Opin. Pharmacol.*, 2014, **18**, 18–27.
6 B. H. Kim, *et al.*, *J. Am. Chem. Soc.*, 2011, **133**, 12624–12631.
7 H. B. Na and T. Hyeon, *J. Mater. Chem.*, 2009, **19**, 6267–6273.
8 Y. K. Peng, *et al.*, *Mater. Today*, 2016, **19**, 336–348.
9 J. Bremerich, *et al.*, *Eur. Radiol.*, 2007, **17**, 3017–3024.
10 M. Lewis, *et al.*, *J. Med. Imaging Radiat. Oncol*, 2012, **56**, 187–191.
11 I. Fernández-Barahona, *et al.*, *Inorganics*, 2020, **8**(4), 28.
12 T. Vangijzegem, *et al.*, *Nanotechnology*, 2018, **29**, 265103.
13 Z. Shen, *et al.*, *ACS Nano*, 2017, **11**, 10992–11004.
14 U. I. Tromsdorf, *et al.*, *Nano Lett.*, 2009, **9**, 4434–4440.

15 A. Roch, *et al.*, *J. Magn. Magn. Mater.*, 2005, **293**, 532–539.
16 H. Arami, *et al.*, *Chem. Soc. Rev.*, 2015, **44**, 8576–8607.
17 C. Cruje and D. B. Chithrani, *Rev. Nanosci. Nanotechnol.*, 2014, **3**, 20–30.
18 C. Boyer, *et al.*, *J. Mater. Chem.*, 2009, **19**, 111–123.
19 C. Boyer, *et al.*, *NPG Asia Mater.*, 2010, **2**, 23–30.
20 F. Alexis, *et al.*, *Mol. Pharm.*, 2008, **5**, 505–515.
21 J. Jokerst, *et al.*, *Nanomed*, 2011, **6**, 715–728.
22 M. J. Ernsting, *et al.*, *J. Controlled Release*, 2013, **172**, 782–794.
23 G. Pasut and F. M. Veronese, *J. Controlled Release*, 2012, **161**, 461–472.
24 S. D. Perrault, *et al.*, *Nano Lett.*, 2009, **9**, 1909–1915.
25 V. D. F. Mosqueira, *et al.*, *Pharm. Res.*, 2001, **18**, 1411–1419.
26 N. Dos Santos, *et al.*, *Biochim. Biophys. Acta*, 2007, **1768**, 1367–1377.
27 N. Gal, *ACS Biomater.*, 2017, **3**, 249–259.
28 R. Gref, *Colloids Surf., B*, 2000, **18**, 301–313.
29 S. D. Li and L. Huang, *J. Controlled Release*, 2010, **145**, 178–181.
30 V. Ntziachristos and D. Razansky, *Chem. Rev.*, 2010, **110**, 2783–2794.
31 A. Hannecart, *et al.*, *Nanoscale*, 2015, **7**, 3754–3767.
32 H. Hyun, *et al.*, *Contrast Media Mol. Imaging*, 2012, **7**, 516–524.
33 D. Forge, *et al.*, *J. Phys. Chem.*, 2008, **112**, 19178–19185.
34 D. Stanicki, *et al.*, *Curr. Opin. Chem. Eng.*, 2015, **8**, 7–14.
35 J. Bridot, *et al.*, *Contrast Medial Mol. Imaging*, 2013, **8**, 466–474.
36 D. Stanicki, *et al.*, *J. Mater. Chem. B*, 2014, **2**, 387–397.
37 D. Forge, *et al.*, *Contrast Media Mol. Imaging*, 2010, **5**, 126–132.
38 C. Cruje and D. B. Chithrani, *Rev. Nanosci. Nanotechnol.*, 2014, **3**, 20–30.
39 K. Rahme, *et al.*, *RSC Adv.*, 2013, **3**, 6085–6094.
40 S. Tenzer, *et al.*, *Nat. Nanotechnol.*, 2013, **8**, 772–781.
41 P. Hahn, *et al.*, *Exp. Gerontol.*, 2009, **44**, 594–600.
42 X. Huang, *et al.*, *Sensors*, 2006, **6**, 756–782.

